

<https://doi.org/10.1038/s43246-024-00508-1>

Structural origins of dielectric anomalies in the filled tetragonal tungsten bronze $\text{Sr}_2\text{NaNb}_5\text{O}_{15}$

Check for updates

Jeremiah P. Tidey¹✉, Urmimala Dey², Ana M. Sanchez¹, Wei-Tin Chen^{3,4}, Bo-Hao Chen⁵, Yu-Chun Chuang⁵, Maria T. Fernandez-Diaz⁶, Nicholas C. Bristowe^{2,8}, Richard Beanland^{1,8} & Mark S. Senn^{7,8}✉

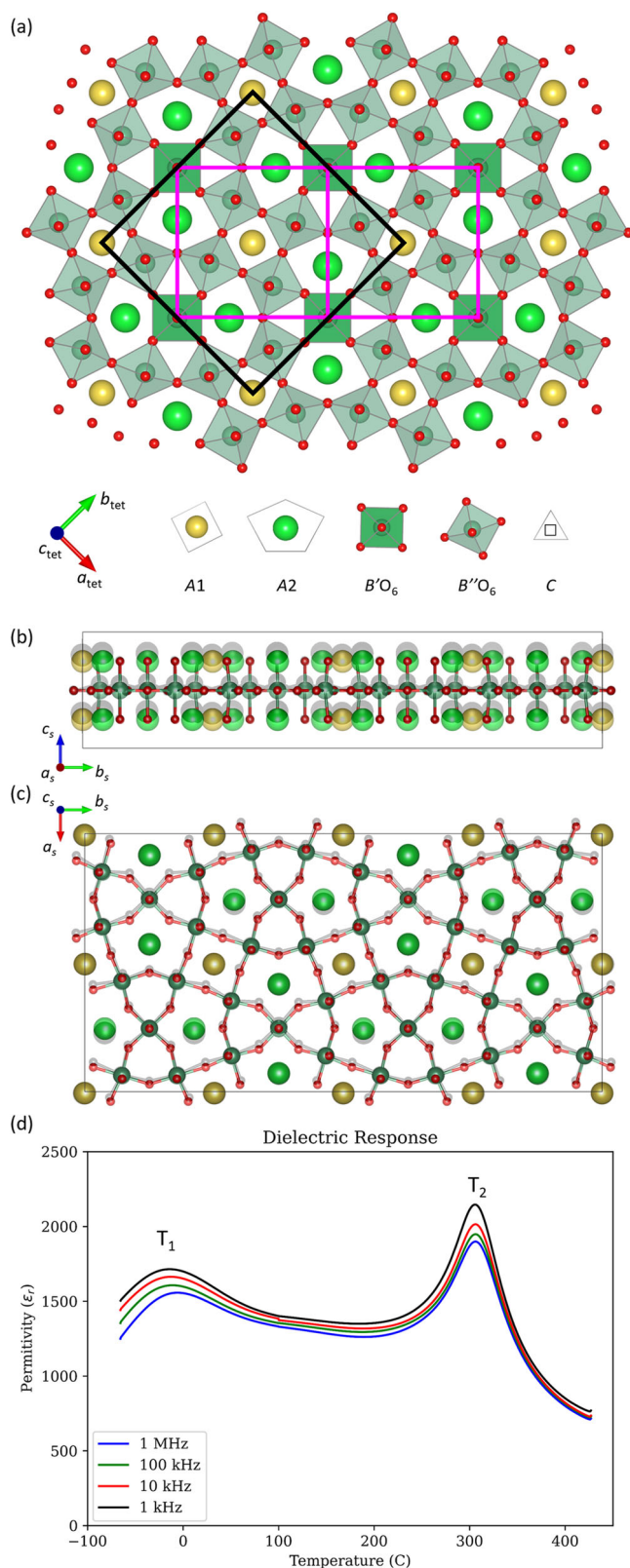
The tetragonal tungsten bronze, $\text{Sr}_2\text{NaNb}_5\text{O}_{15}$, shows promise for application in high-temperature high-efficiency capacitors vital for the sustainable energy revolution. Previously, the structural complexity of this and related materials has obscured the mechanisms underpinning two large anomalies in relative permittivity (ϵ_r) which give rise to their exceptionally broad dielectric response. Here, we comprehensively investigate the structural evolution from -173 to 627 °C, combining electron, X-ray and neutron diffraction, electron microscopy, and first principles electronic structure calculations to unambiguously identify the structural origins of both anomalies. The peak in ϵ_r at 305 °C is associated with a polar-nonpolar phase transition, wherein cations displace along the c axis. Guided by DFT, we identify a further transition upon cooling, associated with the second peak at -14 °C, linked to the softening of an in-plane polar distortion with a correlation length limited by ferroelastic nano-domains arising from rigid-unit-like tilting of NbO_6 octahedra at high temperature, imparting relaxor-like behaviour. Thus, the two dielectric anomalies in $\text{Sr}_2\text{NaNb}_5\text{O}_{15}$ are associated with two distinct crystallographic phase transitions and their interplay with a microstructure that arises from a third, non-polar structural distortion. Chemical control of these will enable development of tuneable materials with dielectric properties suitable for high-temperature energy storage applications.

As global energy supplies shift towards renewable electrics, demand has emerged for high efficiency Class-II capacitors that operate over a wide temperature range, even up to 300 °C^{1,2}. Such devices will require materials with high thermal and chemical stability, high volumetric efficiency and, ideally, constant dielectric properties over the operational temperature range. Current commercial materials are limited in their high-temperature performance, prompting investigation of ceramic relaxor ferroelectrics (RFEs). However, perovskite RFEs with suitable properties generally contain either Bi or Pb which are either toxic or incompatible with the well-established Ni metal electrodes in commercial capacitors. This has triggered investigation into Bi- and Pb-free materials with the tetragonal tungsten bronze (TTB) structure, with materials based on $\text{Sr}_2\text{NaNb}_5\text{O}_{15}$ (SNN)

showing particular promise as a basis for high-functioning dielectrics with appropriate chemical stability, excellent volumetric efficiency, permittivity, and functional range³.

TTBs have the general formula $(A1)_2(A2)_4C_4(B1)_2(B2)_8O_{30}$ and consist of a structure formed of a network of corner-sharing BO_6 octahedra (Fig. 1a–c). Into this, alkali, alkali-earth or transition metals may be intercalated at the 12-coordinate $A1$, 15-coordinate $A2$, and 9-coordinate C sites. The ability to vary both the A - and B -sites allows a wide palette of TTB chemistries exhibiting a range of physical properties that are still under active exploration. The high symmetry, non-polar aristotype structure forms in tetragonal $P4/mbm$ (space group No. 127) and can also be understood as comprising of perovskite-like columns, stacked along c and

¹Department of Physics, University of Warwick, Gibbet Hill Road, Coventry CV4 7AL, UK. ²Centre for Materials Physics, Durham University, South Road, Durham DH1 3LE, UK. ³Center for Condensed Matter Sciences and Center of Atomic Initiative for New Materials, National Taiwan University, Taipei 10617, Taiwan. ⁴Taiwan Consortium of Emergent Crystalline Materials, National Science and Technology Council, Taipei 10622, Taiwan. ⁵National Synchrotron Radiation Research Center, Hsinchu 30076, Taiwan. ⁶Institut Laue-Langevin, BP 156X, Grenoble F-38042, France. ⁷Department of Chemistry, University of Warwick, Gibbet Hill Road, Coventry CV4 7AL, UK. ⁸These authors jointly supervised this work Nicholas Bristowe, Richard Beanland, Mark S. Senn. ✉e-mail: jere.tidey@warwick.ac.uk; m.senn@warwick.ac.uk



centred on the A1 cation. These form the basis of two enantiomorphic structural units which arrange in a checkerboard pattern (magenta boxes, Fig. 1a). Although real TTBs generally have lower symmetries at room temperature than the aristotype, for simplicity we use Miller indices corresponding to the tetragonal aristotype unit cell throughout, unless otherwise stated.

Fig. 1 | Basic material properties. **a** A [001] projection of the aristotype TTB structure with tetragonal $P4/mbm$ symmetry. The unit cell of the tetragonal aristotype is outlined in black; magenta boxes emphasise the mirror planes present in the aristotype to outline enantiomorphic structural units. **b** $[100]_{\text{supercell}}$ and **(c)** $[001]_{\text{supercell}}$ projections of the Γ_3^- and Γ_5^- distortions, respectively, as found in the supercell, showing the distortions as greyed overlays on the undistorted structure which is coloured according to **(a)**. Note the concerted shift parallel to c_s of all oxygen sites relative to the metal centres in **(b)**, and parallel to a_s in **(c)** with significant additional distortion of the A2 sites for which the long axis aligns parallel to a_s . **d** Plot of the dielectric response in SNN, replotted with permission (© 2021 Elsevier) from ref. 3.

In SNN, which has been discussed since as early as the late 60s^{4,5}, $B = \text{Nb}$, $A = \text{Sr}$ and Na , and the C-site is nominally vacant. The tetragonal aristotype cell has dimensions $a_{\text{tet}} = b_{\text{tet}} \approx 12.35 \text{ \AA}$, $c_{\text{tet}} \approx 3.89 \text{ \AA}$. This compound is the basis of a family of promising materials^{3,6} with high relative permittivity, ϵ_r . As shown in Fig. 1d and previously reported³, SNN has two peaks in ϵ_r across the commercially relevant temperature range of -55 to $350 \text{ }^\circ\text{C}$. There exists a relaxor ferroelectric peak, centred at $-14 \text{ }^\circ\text{C}$ at 1 kHz, that shifts to slightly higher temperature with increasing frequency and, at $305 \text{ }^\circ\text{C}$, the more prominent ferroelectric peak. These phenomena are denoted T_1 and T_2 , respectively. While some limited control of these features has been demonstrated via cation substitutions^{3,7}, little is understood about their precise origin or interplay with the chemistry and structure of these materials. Better knowledge of the structure-property relationship is, therefore, essential to improve the viability of TTB materials for commercial applications.

Progress in the understanding of TTBs has been largely empirical to date. Links have been made between the occurrence of incommensurately modulated phases, shown to be associated primarily with octahedral tilting⁸⁻¹⁰, with relaxor ferroelectricity, and the associated understanding that the A1-site tolerance factor presents a significant driving force for the distortion of the NbO_3 network¹¹. A broad sweep of correlations has also been highlighted between relaxor/ferroelectric behaviour and occurrence of commensurate/incommensurate phases of TTBs with a modified¹² tolerance factor (specifically of the A1 site), the average A-site cation radius, and the degree of A and C site filling¹³. However, any transition that lowers symmetry from point group $4/mmm$ inevitably results in merohedral or pseudo-merohedral twinning, significantly complicating the interpretation of bulk 3D diffraction data. Where structural distortions in TTBs are small, they impart only subtle modifications to diffraction patterns that are easily mismodelled or overlooked. Moreover, microstructure and crystallite size have been shown to have an impact on the properties of these materials¹⁴, arguably requiring structure and property to be thoroughly assessed concurrently on the same samples if reliable trends are to be drawn.

Ferroelectricity in lead-free TTBs is generally taken as being produced by large, off-centre displacements of B-site cations (see Fig. 1b, c) that give rise to the often-observed polar nature of the phases at room temperature. Meanwhile, A-site cation displacements are also known to contribute to the polarisation of lead-based TTBs¹⁵. While it seems reasonable to assume that the dielectric anomalies observed in these materials are related to their tendency to exhibit such instabilities, the interconnected BO_6 octahedra also allow a variety of tilt, rotation and cation-shifting patterns^{16,17} which can couple to those polar instabilities. Furthermore, the incommensurate phases which many TTBs form add significant complexity to their crystallographic analysis. All of this complexity has contributed significantly to TTBs remaining less well understood than their ferroelectric perovskite counterparts¹⁸.

In the case of SNN, as was recently discussed¹⁹ and clarified²⁰ for the barium analogue, conflicting reports exist for the identity of the room temperature structure. Several studies propose orthorhombic $Im2a$ in the cell basis $\{(2, -2, 0), (2, 2, 0), (0, 0, 2)\}$ ^{6,7,21}, and this symmetry has also been reported for other TTBs, such as unfilled $\text{Ba}_4\text{L}_{0.67}\text{Nb}_{10}\text{O}_{30}$ compounds ($L = \text{La}, \text{Nd}, \text{Sm}, \text{Gd}, \text{Dy}, \text{Y}$)²². Other reports support an orthorhombic phase for SNN in cell basis $\{(1, -1, 0), (1, 1, 0), (0, 0, 1)\}$ ^{4,5,23}, while some recent

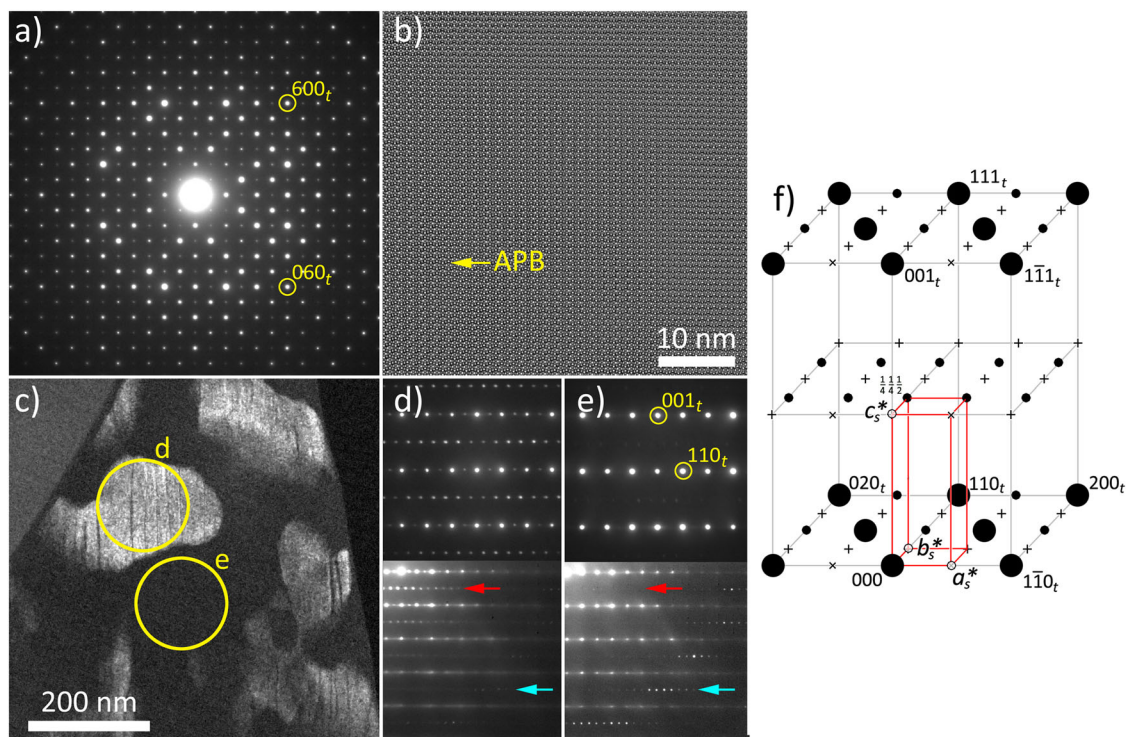


Fig. 2 | Electron microscopic results. **a** SAED pattern along [001] with the same orientation as Fig. 1a, indexed according to the tetragonal unit cell. Faint superstructure reflections are clearly visible at $h \pm \frac{1}{2}, k \pm \frac{1}{2}, 0$. **b** High resolution [001] TEM image (Bragg filtered to reduce noise, see Supplementary Fig. 2, 3). **c** Dark field TEM image taken using ZOLZ superstructure peaks at $l \pm \frac{1}{2}$ at the [110] zone axis, showing bright regions with, and dark regions without, those superstructure peaks. **d, e** The corresponding SAED patterns. Top: the centre of the pattern (ZOLZ) showing the presence (**d**) and absence (**e**) of $h \pm \frac{1}{2}, k \pm \frac{1}{2}, l \pm \frac{1}{2}$ superstructure peaks.

Bottom: the same patterns at lower camera length showing the complementary observation of superstructure peaks in the ZOLZ (red arrow) and FOLZ (cyan arrow). **f** Reciprocal lattice of SNN constructed from (a), (d) and (e) and considering also data from the [113] zone axis (Supplementary Fig. 6). Large circles = aristotype reflections; small circles = superstructure reflections; $\times, +$ = systematic absences due to a -glide and A-centring, respectively; reciprocal lattice vectors of the supercell are marked a_s^*, b_s^*, c_s^* ; red cuboid indicates reciprocal supercell; grey lines added to guide the eye.

studies^{3,24} find no evidence to support anything but the polar tetragonal phase, $P4bm$. If any progress is to be made in understanding the structure-property relationship in this class of materials, it is clearly important to resolve the true structural identity of the system.

Here, we perform a detailed investigation of the structural evolution of SNN from -173 to 627 °C. We combine electron microscopy, electron, X-ray and neutron diffraction techniques, and first principles electronic structure calculations to unambiguously identify the room-temperature structure as an incommensurate, octahedrally tilted phase which approximates closely to an orthorhombic $Ama2$ phase in cell basis $\{(1, -1, 0), (2, 2, 0), (0, 0, 2)\}$. The system undergoes a polar-nonpolar phase transition upon heating around T_2 without significant change to the incommensurate modulation or the amplitude of the tilt order parameter, approximated by A_{am} of the same cell basis. With the help of DFT, we identify a further transition upon cooling below T_1 that comprises of a structure that is very well approximated by the commensurate monoclinic Aa , again in the same cell basis. This result is confirmed by low-temperature neutron power diffraction data. This sequence of phase transitions is consistent with our DFT total energy predictions and group theoretical analysis, enabling us to assign the primary order parameters which drive these transformations. The two anomalies in the permittivity of SNN are hence shown to be associated with two distinct structural phase transitions (order parameters), the chemical control of which will enable the development of tuneable materials with suitable dielectric properties for applications in high-temperature capacitors and energy storage devices. The methods we apply, correlating distortion modes with readily accessible structural parameters (i.e., cell parameters), provide a powerful framework through which the structural driving forces that underlie functional properties in SNN and similar materials can be understood.

Results and discussion

Room-temperature structure determination

An [001] selected area electron diffraction (SAED) pattern, from a region several hundred nm in diameter, is shown in Fig. 2a. Weak superstructure peaks at $h \pm \frac{1}{2}, k \pm \frac{1}{2}, 0$ are clearly visible, suggesting a supercell of at least $\sqrt{2}a \times \sqrt{2}a$ in size, i.e., with cell basis $\geq \{(1, -1, 0), (1, 1, 0), (0, 0, 1)\}$. Any systematic absences, arising from non-symmorphic symmetry elements, i.e., glide planes or screw axes, would be hidden by multiple scattering of the electron beam and/or twin convolution of the pattern. Equally, the lack of splitting in the reflections indicates any strain between twin variants to be below the detection limit of SAED (Supplementary Fig. 1) and, therefore, further symmetry assignment from this diffraction pattern is precluded. At a smaller scale, high resolution (HREM) imaging at the same [001] orientation shows the existence of two non-merohedral twin domains related by a 90° rotation (Fig. 2b, see also Supplementary Figs. 2-3). Periodicity is doubled along [110] or $[1-10]$ in the two regions, with vertical stripes on the bottom left and horizontal stripes at the top and right. An anti-phase boundary (APB) lying on a (110) plane is indicated. Fourier transforms of the two different regions of the HREM image show systematic absences indicative of further symmetry in the structure (Supplementary Fig. 4).

The density of the reciprocal lattice at the [001] projection precludes dark field TEM imaging using the superstructure reflections. However, other zone axes have sufficiently widely spaced reflections to allow their selection with a small objective aperture, as shown in Fig. 2c at the [110] zone axis. This dark field image reveals the regions with superstructure reflections as bright domains with sizes up to a few hundred nm, while regions lacking them remain dark. Anti-phase boundaries along (110) are visible in the bright regions as sharp dark vertical lines, with a spacing that is variable but typically a few tens of nanometres. The convoluted and curved boundaries

(visible also in brightfield TEM, shown in Supplementary Fig. 5) indicate the domain walls incur a very low energy penalty. In Fig. 2d, e, superstructure reflections lie at $h \pm \frac{1}{4}, k \pm \frac{1}{4}, l \pm \frac{1}{2}$ positions in the (110) zero-order Laue zone (ZOLZ) for the bright domains (red arrow), while the dark domains have a higher order Laue zone comprised of $h, k, l \pm \frac{1}{2}$ and $h \pm \frac{1}{2}, k \pm \frac{1}{2}, l \pm \frac{1}{2}$ reflections (cyan arrow). This behaviour is consistent with two domains of a single-face centred lattice, related by a 90° rotation about [001] (as observed directly in Fig. 2b). In such a case, these reflections can be denoted $\pm(h + \frac{1}{4}, k + \frac{1}{4}, l \pm \frac{1}{2})$ in the zero order Laue zone of Fig. 2d, and $\pm(h + \frac{1}{4}, k - \frac{1}{4}, l \pm \frac{1}{2})$ in the first-order Laue zone of Fig. 2e.

Together with a similar dark field + SAED experiment at the [113] zone axis (Supplementary Fig. 6), these results allow the reciprocal lattice for a single domain to be constructed (Fig. 2f, see also Supplementary Fig. 7, 8). As already noted, the superstructure reflections in Fig. 2a imply a reciprocal unit cell of at least basis $\{(1, -1, 0), (1, 1, 0), (0, 0, 1)\}$. The complementary nature of the superstructure reflections in Fig. 2d, e then show the existence of additional centred reflections at the *A*-face, while not at the *B*-face, of this reciprocal unit cell. Finally, where the $h \pm \frac{1}{2}, k \pm \frac{1}{2}, l$ reflections are absent in Fig. 2e and recovered at the [113] zone axis (Supplementary Fig. 6), a glide plane with translational component $[\frac{1}{2}, -\frac{1}{2}, 0]$ is implied. The lattice is, therefore, *A*-centred in cell basis $\{(1, -1, 0), (2, 2, 0), (0, 0, 2)\}$, having an *a* mirror-glide plane perpendicular to the *b* axis. In the presence of coexisting non-merohedral twins, this result explains the prior assignments for SNN^{6,7,21} of an *Im2a* lattice in cell $2a_s, b_s, c_s$ (i.e., with reference to our proposed supercell). However, our data shows that such a case is ruled out by the absence of reflections at $h \pm \frac{1}{4}, k \pm \frac{1}{4}, l$ at $l > 0$.

Orthorhombic lattice symmetry is trivially established by means of a Pawley fit to the high-resolution synchrotron powder diffraction data. Taken together with the likely polarisation of the *c* axis²⁵ and the above electron microscopy and diffraction results, the only possible subgroup, as identified through the use of ISODISTORT^{26,27}, is *Ama2* with cell basis = $\{(1, -1, 0), (2, 2, 0), (0, 0, 2)\}$ and origin shift (0,0,0). As there is only one *Ama2* subgroup of *P4/mbm* with the cell basis determined by our ED data, this is a unique solution. It is not surprising that previous works proposed different assignments^{4-7,21,23,24}, given the small length scale of the twinning (~ 200 nm; see Fig. 2c and Supplementary Fig. 6a), the weak superstructure reflections, and the small deviation from tetragonal metric symmetry. Our *Ama2* model has been identified as the most physically reasonable subgroup for describing rigid unit type tilting of the NbO₆ octahedra^{16,19} and has also been observed in other rigorous studies of TTB structure, particularly in approximations of an incommensurate phase^{8,9,11,13,28}. For example, Ba_{0.61}Pb_{0.39}Nb₂O₆, adopts a near-commensurate *Ama2* structure and also has non-merohedral twinning and similar domain sizes to those found here¹³. These domains are significantly larger than those recently reported for the uniaxial relaxor ferroelectric, Sr_{0.61}Ba_{0.39}Nb₂O₆ (~ 5 nm), which adopts an incommensurately modulated, mixed structure, consisting of slabs of commensurate *Ama2* with another system of periodicity $1.5\sqrt{2}a^{10}$.

Rietveld refinement of powder X-ray diffraction data was then performed in the commensurate *Ama2* space group using a symmetry-adapted displacement formalism²⁹, giving a structure with 145 positional degrees of freedom for 64 independent atoms. These can equally be described by 145 unique distortion modes spanning the eight irreducible representations (irreps) $\Gamma_1^+, \Gamma_4^+, \Gamma_2^-, \Gamma_3^-, M_5^+, M_5^-, S_1$ and S_3 . However, by implementing symmetry based and DFT based constraints, it is possible to reduce the number of free parameters from 145 to 14 (see Methods for further details).

This model provides an improved fit to the data compared to all previously reported models. However, splitting and/or small shifts that were not present for aristotype peaks are evident for superstructure reflections at $\mathbf{k} = [\frac{1}{4}, \frac{1}{4}, \frac{1}{2}]$ (Supplementary Fig. 9a)). It was not possible to resolve these discrepancies by further symmetry lowering, i.e., monoclinic and triclinic subgroups of *Ama2*. We consequently performed a Pawley refinement that allowed the existence of an incommensurate propagation vector, \mathbf{k}_i , to describe the position of the superstructure peaks. Notably, we find that the pattern can be well-fit by considering only the first-index satellite reflections belonging to the propagation vector $\mathbf{k}_i = [\mathbf{q}_i, \mathbf{q}_i, \frac{1}{2}]$, $\mathbf{q}_i = 0.2435$, in addition

to those at $[h, k, l]$ (Supplementary Fig. 9b). Hence, while the electron diffraction and microscopy in isolation is consistent with a commensurate *Ama2* description of the sample, taken together with our PXRD it must be concluded that the bulk adopts instead a closely related incommensurately modulated structure.

Our calculated phonon dispersion curves from DFT, starting from a fully relaxed *P4/mbm* unit cell of SNN, are consistent with the experimentally determined structures and observed incommensurability. Polar instabilities at the Γ -point are revealed by phonons with imaginary frequencies, alongside several non-polar instabilities at other zone-boundary points (Supplementary Fig. 10a, 11a). The polar Γ -point instabilities are found to possess two different characters, transforming as the irreps Γ_3^- and Γ_5^- .

Our DFT calculations (discussed further in Supplementary Information Section B, Supplementary Discussion) reveal that the most unstable phonon mode transforms as the $\Gamma_3^-(a)$ irrep in the *P4/mbm* structure, consistent with our structural refinements. The Γ_3^- mode leads to polar displacements of the cations, relative to the anionic oxygen network, along [001] and gives rise to spontaneous polarisation parallel to the *c* axis (see Fig. 1b). Freezing this mode into our DFT relaxed structures lowers the symmetry to *P4bm*. The phonon spectrum for the resulting polar phase shows the Γ , M and X-point instabilities are significantly reduced, compared to the parent phase, while large, nonpolar instabilities remain at the A, R, Z and S-points of the Brillouin zone (Supplementary Figs. 10b, 11b). Of these, the most unstable phonon mode is nonpolar and found to possess S_3 character, again consistent with the primary order parameters anticipated for the *Ama2* phase from our structural refinements. Further computation of the phonon frequencies in the *P4/mbm* cell along the Z (0, 0, $\frac{1}{2}$) – S' (0.15, 0.15, $\frac{1}{2}$) – S ($\frac{1}{4}, \frac{1}{4}, \frac{1}{2}$) direction confirm that the S_3 mode softens at a k-point that is slightly incommensurate in nature (Supplementary Fig. 10c), consistent with our Pawley refinements of the X-ray diffraction data. However, further resolution of the exact incommensurate modulation vector and relaxation of this structure would require a computationally intractable supercell. Hence, although DFT also suggests a slight incommensurability of the S_3 order parameter in SNN, we retain the commensurate approximation to allow our experimental model to be constrained by our calculations. Nevertheless, for completeness, we provide the full incommensurate space group assignment as *Cmm2*(0,*g*, $\frac{1}{2}$)000 in the cell basis $\{(-1, 1, 0, 0), (-1, -1, 0, 0), (0, 0, 1, 0), (0, 0, 0, 1)\}$ and origin shift ($\frac{1}{2}, 0, 0, 0$) (see Methods for full details).

The *Ama2* structure obtained from the condensation of the $S_3(a, 0; 0, 0)$ mode in the *P4bm* structure is fully relaxed from DFT and compared with the experimental crystal structure observed at room temperature (see also Supplementary Information Section B, Supplementary Discussion). As discussed previously, subsequent analysis of the diffraction data is performed using the DFT constrained model, since this greatly reduces the parameter space without a significant cost to the quality of fit. We find good agreement between our DFT-optimised *Ama2* structure and the freely refined room temperature PXRD model in terms of lattice parameters ($\Delta \leq 0.6\%$), cell volume ($\Delta \leq 0.7\%$), and model amplitudes (Supplementary Table 1). The room temperature model, refined against the diffraction data, confirms the mode transforming as S_3 to have the largest associated distortion, with magnitude $A_p \sim 2.0 \text{ \AA}$, as defined in ISODISTORT^{26,27}, followed by the ferroelectric Γ_3^- distortion ($A_p \sim 0.47 \text{ \AA}$). The S_3 irrep constitutes a complex RUM distortion upon the NbO₆ network, alongside non-polar, in-plane displacements of the A-site cations which occur antiparallel between subsequent (001) layers and so are of no direct consequence to the dielectric properties. Of the remaining distortions, only those relating to strain show significant activity, while the piezoelectric Γ_2^- mode has an amplitude roughly 100 times less still. While it is essentially inactive across our study (see Fig. 3a), with only a very small component developing as the sample is cooled below T_1 , we retain the Γ_2^- irrep in our model since it has previously been described as presenting important competition with ferroelectric modes in Sr_{0.61}Ba_{0.39}NbO₂¹⁰ and the more closely related, filled TTB,

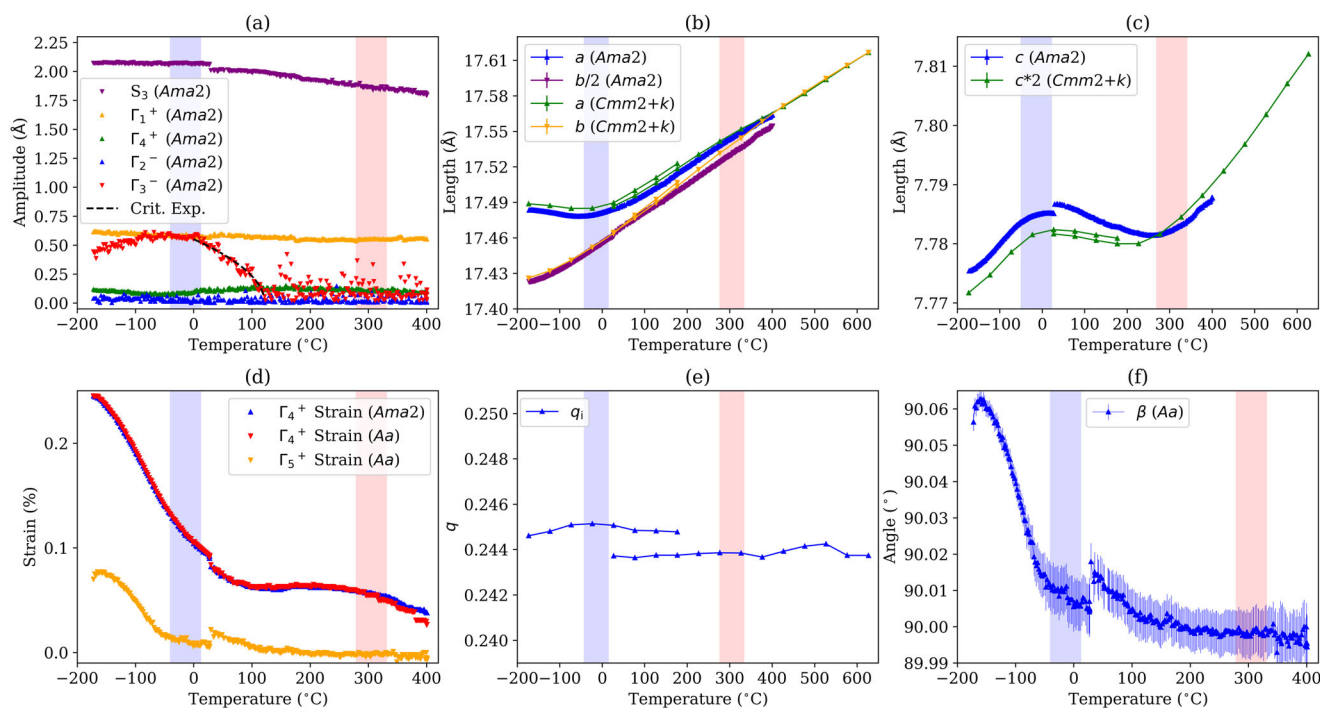


Fig. 3 | Powder diffraction results. Plots of the temperature evolution of (a) the displacive distortion amplitudes for the *Ama2* model (five outlying data points removed across two temperatures where refinements adopt false minima; see Supplementary Fig. 16b for full data), and with a critical exponent fit assuming second-order behaviour shown for Γ_3^- above 0 °C ($T_c = 121.8(13)$ °C); (b) *a* and *b* and (c) *c* axis cell lengths from VT-PXRD Rietveld refinements using data from Diamond Light Source (*Ama2* and *Aa* models) and Taiwan Photon Source (*Cmm2+k* Pawley refinement); (d) symmetry-adapted strains; (e) incommensurate component of the propagation vector, \mathbf{k}_i , for the observed superstructure, presented with respect to the

tetragonal cell; and (f) β angle in the *Aa* model. Regions corresponding to the T_1 and T_2 maxima in permittivity are highlighted in blue and red, respectively. Error bars are present and show the 3σ standard uncertainty for (b), (c), and (f); for clarity they are omitted and in the order of 10% for non-zero mode values in (a) and (d) and ~ 0.015 for (e), while the systematic trends give better estimate of the true precision. For both datasets, high-temperature data were collected first, with temperature increasing, followed by low-temperature data, also with temperature increasing; the discontinuity between low and high-temperature sweeps is due to hysteresis in sample behaviour.

$REK_2Nb_5O_{15}$ ($RE = \text{Rare Earth}$)³⁰. Supplementary Fig. 12 shows the final refined structure at room temperature, including depiction of the S_3 tilt mode, and the refined A-site cation disorder and its discussion (see also Supplementary Fig. 13–15).

Thus, we have shown that, at RT, while SNN actually adopts an incommensurately modulated structure, it can very satisfactorily be described with the commensurate approximation of *Ama2* with basis $\{(1, -1, 0), (2, 2, 0), (0, 0, 2)\}$, origin shift $(0, 0, 0)$, in terms of the observed ED and PXRD data and supported by theoretically calculated phonon instabilities and relaxed structures. This model captures the salient features of the polarisation, octahedral tilting, and their coupling to lattice strain. In the following discussion we interrogate this model via variable temperature (VT) PXRD and further comparison with DFT to reveal the structural origins of the dielectric anomalies in SNN.

Variable temperature structure analysis

Analysis of the temperature-dependent evolution of structure shows three distinct regions, approximately bounded by the T_1 and T_2 peaks in permittivity (Fig. 3, see also Figure 1d)³. Above T_2 , all unit cell lengths (Fig. 3b, c) show positive thermal expansion and the orthorhombic distortion is particularly small (symmetry-adapted orthorhombic strain, $|\Gamma_4^+| < 0.06\%$, Fig. 3d), diminishing steadily with increasing temperature as the system tends to a pseudo-tetragonal state within the estimated uncertainties. As temperature drops below T_2 , the orthorhombic strain saturates at $e_{\text{ortho}} \sim 0.1\%$ and a modest negative thermal expansion (NTE) of the *c* axis (Fig. 3c) develops with coefficient $\alpha = -3.3$ ppm between 60 °C and 250 °C. While this NTE occurs over a similar temperature range as has been reported for $Ba_2NaNb_5O_{15}$, it is an order of magnitude smaller, with $\alpha \sim -33$ ppm reported for BNN between ~ 410 – 590 °C³¹.

The region over which the polar Γ_3^- distortion amplitude saturates (Fig. 3(a)) coincides well with the bounds of the region in which the *c* axis exhibits NTE (Fig. 3c), and the behaviour of the cell parameters corresponds well with the trends in the symmetry-adapted distortions. The ferroelectric Γ_3^- distortion refines to near zero values above T_2 and the distortion reaches a maximum magnitude, A_p , of approximately 0.6 Å around T_1 , below which temperature it appears somewhat reduced. This behaviour is reminiscent of other classical ferroelectrics, where a polar distortion drives NTE along the polar dimension until the distortion is saturated^{32–34}.

While we do not investigate the thermal behaviour of the material, the critical exponent fit against the amplitude of the Γ_3^- polar distortions refines to 0.58(3) indicating a likely second-order transition (constrained fit shown in Fig. 3a). This clearly associates the T_2 phenomenon to a softening of the Γ_3^- mode. We thus identify a second-order phase transition between *Ama2* and *Amam*, with the cell bases retained (else between *Cmm2*($0, g, \frac{1}{2}$)000 and *Cmmm*($0, g, \frac{1}{2}$)000 in the incommensurate description). From a materials design perspective, such phase transitions are more desirable than their first-order counterparts since they allow for smooth and continuous variation of properties, for example with temperature or chemical substitution. This is in contrast to the case of BNN, in which the equivalent high-temperature ferroelectric transition is first-order in nature³¹.

Assuming a second-order phase transition, gives a critical temperature $T_{\text{crit}} = 121.8(13)$ °C, ~ 130 °C lower than the high-temperature limit of the NTE of the *c* axis and ~ 180 °C lower than the dielectric anomaly at T_2 . It hence seems likely that local fluctuations in the Γ_3^- mode may drive NTE of the *c* axis as the mode softens, but before the correlation length of these distortions becomes sufficiently large for a phase transition to be observed in the intensities of a diffraction experiment. Furthermore, we find that the *c* lattice parameter is increased in the DFT-relaxed *Ama2* phase, compared

Table 1 | Structural details for the elucidated phases

Space group (Condensed irreps)	SNN						BNN ³¹	
	<i>a</i> (Å)	<i>b</i> (Å)	<i>c</i> (Å)	<i>S</i> ₃ (Å)	Γ_3^- (Å)	Γ_5^- (Å)	Relative energy per 46-atom unit cell (eV)	
<i>P4/mbm</i>	12.470	12.470	3.939	–	–	–	0.00	0.00
<i>P4bm</i> (Γ_3^- (<i>a</i>))	12.437	12.437	3.996	–	1.4273	–	–0.20	–0.41
<i>Amam</i> (<i>S</i> ₃ (0, 0; <i>a</i> , 0))	17.507	35.117	7.674	2.3353	–	–	–1.36	–
<i>Ama2</i> (Γ_3^- (<i>a</i>) \oplus <i>S</i> ₃ (<i>a</i> , 0; 0, 0))	17.450	34.826	7.809	2.3440	0.8499	–	–1.50	–0.54
<i>Aa</i> (Γ_3^- (<i>a</i>) \oplus Γ_5^- (<i>a</i> , <i>a</i>) \oplus <i>S</i> ₃ (<i>a</i> , 0; 0, 0))	17.615	34.828	7.752	2.2820	0.5881	0.8905	–1.63	–

Space groups, lattice parameters, select A_p values for distortion amplitudes, and relative energies of child structures obtained by the condensation of unstable phonon modes in the parent *P4/mbm* phase. Relative energy values for BNN are taken from ref. 31.

to that for *Amam* (See Table 1), consistent with the experimentally observed NTE being driven by this sequence of phases. We conclude that the temperature dependence of *c* may provide a useful diagnostic tool with which to interrogate the Γ_3^- distortion, even in instances where high-quality diffraction data are not readily available.

We note the invariance with temperature of the octahedral tilt system, *S*₃, in both amplitude (Fig. 3a) and propagation vector (Fig. 3e), which remains present up to the limit of our VT PXRD experiment, 627 °C (Supplementary Fig. 16a). This corroborates our DFT calculations, which indicate the *S*₃ mode to provide by far the greatest contribution to symmetry lowering (Table 1, see also Supplementary Table 3) and, therefore, being expected to condense at much higher temperatures than the other primary order parameters. Hence, the rigid unit mode is unlikely to contribute directly to the dielectric anomalies in SNN.

We now turn our attention to the structural origin of the *T*₁ phenomenon. While above *T*₁ there is a modest, monotonic depletion of *S*₃ from $A_p \approx 2.04$ Å to a minimum value of $A_p \approx 1.82$ Å at 400 °C, below *T*₁ there is no significant evolution of the mode amplitude. On the other hand, orthorhombic strain begins to evolve, driven primarily by a modest NTE along the *a* axis of the supercell. Alongside further changes in the lattice parameter gradient below *T*₁ and the diminishing of the structural distortions transforming as Γ_3^- , this indicates the possibility of another phase transition at low temperature. Earlier dielectric experiments^{36,7} in SNN also point to the presence of another polar phase at low temperature.

To investigate the nature of a second polar phase at low temperature, we calculated Γ -point phonons for the *Ama2* structure which revealed the presence of further unstable polar modes, transforming as the Γ_5^- (*a*, *a*) irrep (labelled with respect to the *P4/mbm* phase). The doubly degenerate Γ_5^- irrep corresponds to polar displacements of atoms along the [110] direction, necessarily in phase between (001) layers, with a concerted rotation of the NbO₆ octahedra about axes parallel to *c*, and is associated with ferroelectric polarisation in the *ab*-plane (see Fig. 1c). Our DFT relaxed structures show that, unlike the Γ_3^- modes where all atoms share a similar displacement, the Γ_5^- modes harbour a significantly greater distortion at A2 sites with their long axis aligned to the *a* axis compared to that of those for which this is aligned to the *b* axis (see also Fig. 1). Thus, the character of the Γ_5^- mode can be viewed as being dominated by the displacement of these A2 sites. This is of potential significance since we find evidence of cation ordering between A1 and A2 sites (see Supplementary Figs. 12–15), and the occurrence of differing size and charge density at those sites would likely have further interplay with the ferroic properties of the material. In this context, understanding how to control A-site cation order/disorder at in the TTB structure should provide specific means to tune the character of the dielectric anomaly at *T*₁. Indeed, there is evidence in the literature³⁵ that substituting Ca in place of Sr directly affects the in-plane dielectric response of SNN, the origin of which must be the Γ_5^- as evident from our work.

Freezing in the Γ_5^- (*a*, *a*) modes leads to a lower symmetry monoclinic phase in space group *Aa* (basis = {(1,–1,0), (2,2,0), (0,0,2)}, origin shift = (0,0,0)) which is ~ -1.63 eV per 46-atom unit cell more stable with respect to the aristotype and -0.13 eV per 46-atom unit cell more stable compared

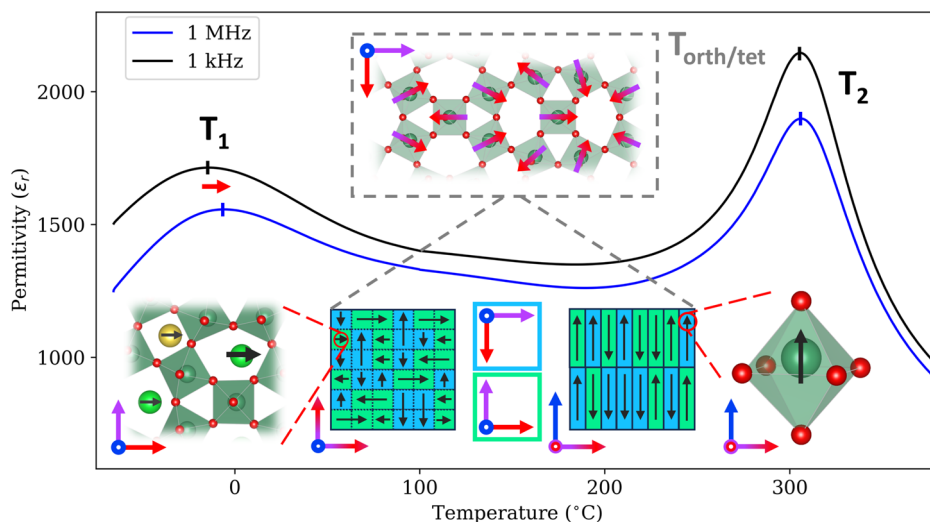
to the *Ama2* phase (see Table 1). As shown in Table 1, competition between the in-plane (Γ_5^-) and out-of-plane (Γ_3^-) polar modes in the *Aa* structure leads to a decrease in the *c* lattice parameter with a simultaneous increase of the *a* lattice parameter due to further coupling of the polarisation and (in-plane) strain along the *a* axis, while the *b* lattice parameter remains almost constant. Notably, these predictions also map on to the observed behaviour of the cell parameters in the PXRD where, below 0 °C, positive thermal expansion resumes in *c* with approximately the same coefficient as above *T*₂, while there develops an increase in orthorhombic strain as the *a* axis undergoes NTE [$\alpha = -2.7$ ppm between -160 and -50 °C] (Fig. 3b), similar in magnitude to that seen for *c* in the *Ama2* phase. Thus, DFT predicts the existence of another proper ferroelectric *Ama2* \rightarrow *Aa* phase transition at lower temperatures in the commensurate approximation.

To corroborate this prediction further, we perform high-resolution neutron powder diffraction at D2B, ILL, affording us greater sensitivity to the subtle oxygen displacements underpinning this phase transition. At room temperature, above *T*₁, there is no meaningful difference between the *Ama2* and *Aa* models, in which only one additional DFT constrained parameter is introduced to account for the polar distortions transforming as Γ_5^- , with the R_{wp} falling by only 0.05% (from 5.21 to 5.16) between the two refinements. By 10 K, this difference in the quality of fits has increased substantially to 0.11% (from 5.33 to 5.22%; data presented in Supplementary Fig. 17). We view this result as being particularly significant as, due to the employed DFT constraints, only one additional refinable parameter is introduced to the *Aa* Rietveld model (a monoclinic lattice distortion is refined in both models in order to keep the comparison as fair as possible).

To better understand the evolution of the phase transition about *T*₁, we consider refinement of a similar symmetry adapted formalism for an *Aa* phase as described above for the *Ama2* phase against the variable temperature synchrotron powder diffraction data. Due to the greater resolution in 2 θ -space, compared to our neutron powder diffraction data, we are able to resolve a small deviation of the β angle from 90 °, that develops only below *T*₁ (Fig. 3f). This would appear to further support the existence of the DFT predicted monoclinic *Aa* phase. However, this is small ($90^\circ + \Delta_{\max} = 90.0618(8)^\circ$) and can equally well be modelled using an anisotropic microstrain peak shape broadening model³⁶ of orthorhombic strain in the *Ama2* phase. Similarly, we find a lack of sensitivity of our data to the distortions constituting the primary order parameter, transforming as Γ_5^- , which brings about the symmetry lowering to *Aa* (else *C1m1*(0,*g*, $\frac{1}{2}$)0, cell basis {(1,–1,0), (1,1,0), (0,0,1,0), (0,0,0,1)} with the origin shift ($\frac{1}{2}$,0,0,0), in the incommensurate description). At temperatures around *T*₁, it is perhaps more appropriate to view the origin of the apparent shear macrostrain as the formation of nanodomains of this additional FE order parameter, but without the long-range coherence to modulate observed X-ray diffraction intensities or produce a coherent distortion of the lattice.

As the in-plane polar distortion of the *Aa* structure, Γ_5^- , lies along the *a* axis of the ferroelastic supercell, its domain structure is constrained by the existing orthorhombic twin domains. These arise from the *S*₃ tilt mode and

Fig. 4 | Structure overview as a function of temperature. Diagram showing (grey dashed box) view, parallel to c , of the asymmetric portion of the S_3 distortion which gives rise to the twin domain structure from very high temperatures, with tilt directions of the apical oxygen atoms shown as purple/red arrows; diagrammatic representations of the domain structure (centre-left and centre-right blue/green squares) coloured with respect to the cell bases shown (centre; a_s red, b_s purple, and c_s blue), and the respective distortions shown alongside, with polarisation directions shown using black arrows, and under the respective portions of the 1 kHz and 1 MHz traces of the permittivity response (replotted with permission (© 2021 Elsevier) from ref. 3) to highlight their relationship to the T_1 and T_2 phenomena.



impose maximum domain sizes of 100–200 nm (Fig. 2c) with pinned 90° domain boundaries (Fig. 2b) firmly limiting the coherence length of the polarisation. Further reduction in domain size for this in-plane polarisation may also result from the APBs (the majority of which have orientations that would correspond to neutral 180° domain walls), as well as the incommensurate modulation and further coupling to the Γ_3^- distortion. Thus, while the ferroelastic S_3 mode is not itself polar, its domain structure still contributes to the relaxor-type behaviour of the T_1 dielectric anomaly. This insight adds weight to the work of Grendal et al.²⁰ where they propose the microstructure in BNN, associated with S_3 , to have a strong influence on the observed spontaneous strain which itself should be strongly coupled to the ferroelectric ordering, providing an explanation to the association of incommensurate modulation with relaxor behaviour.¹³ The situation for the Γ_3^- distortion (polar along the c axis, softening at T_2) is quite different since the c axis is already symmetry unique in the aristotype and, therefore, any further domain structure does not affect its coherence. The relationship between the ferroelastic and ferroelectric domain structures is depicted in Fig. 4.

It is hence imperative to understand the chemical control all three of these structural distortions to tune the dielectric response for high-temperature energy storage applications. Given that the in-plane polar distortion has a significant contribution from off-site $A2$ cations, substitutions on the $A2$ site should be promising for controlling the position of T_1 . On the other hand, T_2 has a strong coupling to out of plane thermal expansion (i.e., NTE is observed on cooling below T_2) and so might be pushed to higher temperatures by cation substitutions that reduce the unit cell volume. Thus, systematic studies investigating the variation of cation size, variance, and polarizability, using the structural insights made available from the temperature dependence of unit cell parameters, should prove insightful as to how the dielectric properties associated with T_1 and T_2 can be tuned effectively. In that context, the addition of Raman spectroscopy might add yet further insight to the subtle structural behaviour. Such work has been undertaken in functional perovskite materials where defects have been shown to tune the occurrence and nature of antipolar displacements.³⁷

Conclusions

Thus, we have shown that the two dielectric features in SNN, which are intimately linked with the material's ability to meet specifications with respect to use as a high-temperature dielectric, are concomitant with structural macro and microstrains, as observed through our high-resolution VT PXRD. T_2 clearly coincides with the onset of NTE upon cooling and our structural refinements are supported by DFT calculations in describing a long-range phase transition from polar $Ama2$ to non-polar $Amam$ in the commensurate description with heating. At lower temperatures, T_1 has

much more subtle origins but DFT calculations, taken together with low-temperature neutron powder diffraction refinements and observed microstrains, suggest its origin is due to a second FE instability with limited coherence length. This limited coherence length is provided by the ferroelastic domain structure resulting from a third instability of the parent structure corresponding to rigid-unit-like tilting of the NbO_6 octahedra. DFT further shows the in-plane polar mode to have dominant character associated with the off-center displacement of select 15-coordinate $A2$ cations, making them a key target for chemical control of the T_1 relaxor anomaly. The identification of these specific structural descriptors for the dielectric anomalies paves the way towards the systematic assessment and optimisation of the desired dielectric properties and their dependence on chemical substitutions.

Methods

The sample of SNN studied here by XRD and electron techniques is precisely that used in the study by Brown et al.³, while additional sample was required to achieve the neutron study, synthesised by the same method reported therein.

Electron microscopy

For transmission electron microscopy (TEM) and scanning-TEM (STEM), SNN powder was mixed with fine (<10 μm) aluminium powder in a ratio 1:10 and pressed using cold rollers to form a sheet $\sim 100 \mu\text{m}$ in thickness. This was mechanically thinned to $\sim 20 \mu\text{m}$ and mounted on a copper support ring using epoxy resin before ion milling to electron transparency using Ar^+ ions at 6 keV. The specimen was finished using an ion beam energy of 100 eV to reduce surface damage and provide sufficiently thin edges for S/TEM (see Supplementary Fig. 18). Samples were examined using JEOL 2100 LaB₆ and aberration corrected ARM200F microscopes operating at 200 kV. The detector angles for the ARM200F darkfield images are 45–180 mrad and 0–40 mrad for brightfield, with a convergence angle of 18 mrad.

Powder diffraction measurements

For XRD, the sample was ground and filled into a quartz capillary of 0.3 mm internal diameter. Data were collected at beamline I11 of Diamond Light Source (DLS) using 15 keV radiation collected at a MYTHEN detector for variable temperature (VT) sweeps with a heating rate of 6 $^\circ\text{C min}^{-1}$ ($\lambda = 0.825309(8) \text{ \AA}$ for data -172 to $27 \text{ }^\circ\text{C}$, and $0.8254874(17) \text{ \AA}$ for 29 to $400 \text{ }^\circ\text{C}$). Temperatures were controlled using an Oxford Cryosystems Cryostream and a Cyberstar hot air blower, respectively. Further data were collected on Beamline 19 A at the Taiwan Photon Source (TPS) using 16 keV radiation ($\lambda = 0.7748842(17) \text{ \AA}$) collected at a MYTHEN detector, temperatures controlled using an Oxford Cryosystems Cryostream (-173

to 177 °C) and an FMB Oxford hot air blower (27–627 °C) with a heating rate of 6 and 12 °C min⁻¹, respectively. In all cases, the sample was rotated during collection for better averaging.

High-resolution neutron powder diffraction data was collected on a second batch of the sample at instrument D2B at the ILL under proposal number 5-23-783³⁸. A beamline standard sample Na₂Ca₃Al₂F₁₄ having space group *I*2₁3 and reference lattice parameter of $a = 10.246116$ was used to determine the experimental wavelength of 1.592736(6) Å and the instrumental contributions to a Thompson-Cox-Hastings pseudo-Voigt peak shape function. Approximately 5 g of the SNN sample was loaded into a vanadium can and cooled in an ILL cryostat down to base temperature. Powder diffraction data were collected upon warming at 1.5, 150, 250 and 295 K, with each scan taking approximately 4 h. The usable data limit for the Rietveld refinement was determined to be 10 to 132 degrees 2θ.

Structural refinements

Refinements of the powder diffraction data were performed in TOPAS Academic Version 7^{29,39} using a symmetry-motivated basis, as parameterised by ISODISTORT^{26,27}. Our refinements were performed in *Ama2*, cell basis $\{(1, -1, 0), (2, 2, 0), (0, 0, 2)\}$, as discussed in the main manuscript. Using distortion modes as refinement parameters²⁹ gave 70 degrees of freedom, spanning the irreducible representations (irreps) S_3 , polar/ferroelectric Γ_3^- , piezoelectric Γ_2^- , and the Γ_1^+ and Γ_4^+ strains. As further discussed below, we constrain the 35 modes spanning the irreps M_5^+ and M_5^- to zero, as well as the 40 modes spanning the irrep S_1 , the inclusion of which otherwise only generated unobserved intensities and served no improvement to the fit. These restrictions are supported by the symmetry analysis of Whittle et al.¹⁶ who determine that the only irrep consistent with a rigid-unit-mode (RUM) type motion in any TTB with a unit cell up to $2\sqrt{2}a \times 2\sqrt{2}a \times 2c$ is S_3 , since other modes distort the NbO₆ octahedra too much to exist in real materials. Their analysis leads them to the same commensurate *Ama2* space group we use here when reviewing existing data on Ba₂NaNb₅O₁₅ (BNN)¹⁹.

The characters of the distortions that transform as each individual irrep were analysed from the relaxed density functional theory (DFT) structures, giving the magnitude of the individual distortion modes. In the final model refined against the diffraction data, the number of additional free parameters introduced into the model to describe the internal atomic coordinates was further reduced to 14 by constraining the relative magnitude of each mode associated with each irrep by using DFT derived ratios, excepting those of the Γ_1^+ irrep which necessarily remain free. Thus, the precise character of each distortion associated with Γ_2^- , Γ_3^- , Γ_4^+ , and S_3 come from our ground state DFT calculations while the overall amplitude is derived from refinement against our diffraction data. These constraints reduce the parameter space of our model greatly (from 155 to 24 parameters in total for the structure) and have only a very modest effect on the quality of the fit to our high-resolution PXRD data (e.g., at 300 K, $R_{wp} = 2.82\%$ vs 2.57%).

The Na and Sr occupancies of the A1 and A2 sites were first refined at each temperature under a constraint that respects the nominal stoichiometry, before being fixed to an average value in the final model. In addition, lattice parameters, peaks shape broadening described by Lorentzian and Gaussian microstrain functions and background parameters were refined using the Rietveld method against PXRD data collected from DLS in the range of 5 to 73 in 2θ or TPS data.

ISODISTORT gives only one incommensurate supersymmetry consistent with primary order parameters Γ_3^- (a) and S_3 that we have identified: *Cmm2*(0, g , $\frac{1}{2}$)000 in the cell basis $\{(-1, 1, 0, 0), (-1, -1, 0, 0), (0, 0, 1, 0), (0, 0, 0, 1)\}$ and origin shift ($\frac{1}{2}, 0, 0, 0$). Here, the symmetry of the parent in *P4/mbm* is first broken to give the commensurate subgroup, *Cmm2*, with new basis $\{(-1, 1, 0, 0), (-1, -1, 0, 0), (0, 0, 1, 0)\}$, and the incommensurate propagation vector, $(0, g, \frac{1}{2})$ where $g \sim 0.487$, is then used to describe the modulation within the superspace (3-D + 1) formalism, made with reference to the new cell basis. Unfortunately, it was not possible to achieve a physically realistic and stable Rietveld refinement of the incommensurate structure using *Jana2020*⁴⁰, no doubt in part due to the large number of refinable degrees of

freedom allowed and correlations therein. Consequently, all structural models were obtained by refinements in a commensurate approximation, i.e., *Ama2* with basis $\{(1, -1, 0), (2, 2, 0), (0, 0, 2)\}$, origin shift (0,0,0).

To interrogate the temperature-dependent evolution of the incommensurate propagation vector, we performed a Rietveld refinement in *Cmm2* (cell basis $\{(1, -1, 0), (1, 1, 0), (0, 0, 1)\}$) with the addition of an incommensurate modulation vector, $\sim [0, 0.487, \frac{1}{2}]$ ($\mathbf{k}_1, \mathbf{k}_2, \mathbf{k}_3$, respectively) with respect to the supercell by using a custom peak fitting function within Topas. The propagation vector and associated intensities were refined on data between 5 and 11° in 2θ using only first-order satellite reflections, since this was the region over which those intensities can be fit without correlation with others. Refinement of the modulation vector showed \mathbf{k}_1 and \mathbf{k}_3 to be commensurate [$\mathbf{k}_1 = 0, \mathbf{k}_3 = \frac{1}{2}$] and consequently only \mathbf{k}_2 was refined in the final model.

We note a small (4% in sample used for X-ray and electron studies, 8% for that of neutrons) NaNbO₃ impurity that is fully included throughout this work. There is an additional, small, unindexed phase, evident in the neutron sample via peaks at 19 and 38° 2θ. These peaks are not evident in the X-ray diffraction data and our good agreement with refinement results against these data suggest our neutron refinement results are robust despite its presence.

First principles calculations

Density functional theory (DFT) calculations were carried out using the projector augmented wave (PAW) method within the Vienna Ab-initio Simulation Package (VASP)^{41,42}, version 6.3.0, employing models with completely ordered Na and Sr occupancy of the A1 and A2 sites, respectively. This imposed ordering was necessary in order to not artificially break the symmetry of our finite-sized simulation cells (under periodic boundary conditions), the sites being chosen according to the relative sizes. We note that it is likely that mixing of these sites would affect the energies of the tilt systems to some degree but deem it an acceptable approximation since the experiment and theory match well throughout. For exchange correlation, we employed the PBEsol version of generalised gradient approximation (GGA)⁴³ which is known to accurately determine the equilibrium properties of bulk systems, especially oxides. PAW pseudopotentials⁴⁴ (PBE, version 5.4) were used for all the calculations with the following valence shell configurations: 4s² 4p⁶ 5s² (Sr), 2s² 2p⁶ 3s¹ (Na), 4p⁶ 4d⁴ 5s¹ (Nb) and 2s² 2p⁴ (O). Convergence tests performed on a 46-atom *P4/mbm* unit cell revealed that a plane wave cutoff of 700 eV and a k -mesh grid of $2 \times 2 \times 6$ were necessary to converge total energies, forces, and stresses to within 1 meV per unit cell, 1 meV Å⁻¹, and 0.02 GPa, respectively. For all calculations, the energy convergence criterion was set to 10⁻⁹ eV. Lattice parameters and atomic positions were fully relaxed until the Hellmann-Feynman force on each atom was less than 0.1 meV Å⁻¹. Phonon calculations were performed using a $\sqrt{2} \times \sqrt{2} \times 4$ phonon supercell employing density functional perturbation theory (DFPT)⁴⁵ implemented in VASP and post-processing was done via PHONOPY⁴⁶. The non-analytical term correction to the dynamical matrices was included to properly account for the LO-TO splitting at the zone centre^{47,48}. Born effective charges and the dielectric tensor were obtained from VASP-DFPT calculations. We used FINDSYM^{49,50} to determine the space group symmetries of the relaxed structures obtained from VASP, while ISODISTORT^{26,27} was employed to find the mode amplitudes and corresponding order parameter directions (OPDs). Complete structural details of the DFT-optimised *Amam*, *Ama2* and *Aa* phases of SNN are given in Section B of the Supplementary Information and Supplementary Tables 2-5.

Data availability

Supplementary Information is available for this paper. DFT-relaxed structures and results of phonon spectra calculations, and all raw (.xye) crystallographic data, along with TOPAS input, output and crystallographic information (.cif) files, as well as the outputs of ISODISTORT analyses where relevant have been made available at DOI: 10.6084/m9.figshare.24279499⁵¹. These may also be obtained from the

corresponding authors by request. Express permission was provided by T. Brown for the reproduction of their electrical data relating to SNN.

Received: 26 January 2024; Accepted: 18 April 2024;

Published online: 07 May 2024

References

- Watson, J. & Castro, G. A review of high-temperature electronics technology and applications. *J. Mater. Sci. Mater. Electron.* **26**, 9226–9235 (2015).
- Li, Q. et al. High-temperature dielectric materials for electrical energy storage. *Annu. Rev. Mater. Res.* **48**, 219–243 (2018).
- Brown, T. et al. New high temperature dielectrics: Bi-free tungsten bronze ceramics with stable permittivity over a very wide temperature range. *J. Eur. Ceram. Soc.* **41**, 3416–3424 (2021).
- Van Uitert, L. G. et al. *Bronze-like Niobates* Vol. 3, 47–57 (Pergamon Press, Inc., 1968).
- Giess, E. A., Scott, B. A., Burns, G., O’Kane, D. F. & Segmüller, A. Alkali strontium-barium-lead niobate systems with a tungsten bronze structure: crystallographic properties and curie points. *J. Am. Ceram. Soc.* **52**, 276–281 (1969).
- Xu, S. et al. Enhanced energy storage properties and superior thermal stability in SNN-based tungsten bronze ceramics through substitution strategy. *J. Eur. Ceram. Soc.* **42**, 2781–2788 (2022).
- García-González, E., Torres-Pardo, A., Jiménez, R. & González-Calbet, J. M. Structural singularities in ferroelectric $\text{Sr}_2\text{NaNb}_5\text{O}_{15}$. *Chem. Mater.* **19**, 3575–3580 (2007).
- Labbe, P., Leligny, H., Raveau, B., Schneck, J. & Toledano, J. C. X-ray structural determination of the quasi-commensurate phase of barium sodium niobate. *J. Phys. Condens. Matter* **2**, 25–43 (1990).
- Woike, T. et al. The modulated structure of $\text{Ba}_{0.39}\text{Sr}_{0.61}\text{Nb}_2\text{O}_6$. I. Harmonic solution. *Acta Crystallogr. B: Struct. Sci.* **59**, 28–35 (2003).
- Krayzman, V., Bosak, A., Playford, H. Y., Ravel, B. & Levin, I. Incommensurate modulation and competing ferroelectric/antiferroelectric modes in tetragonal tungsten bronzes. *Chem. Mater.* **34**, 9989–10002 (2022).
- Levin, I. et al. Coupling between octahedral tilting and ferroelectric order in tetragonal tungsten bronze-structured dielectrics. *Appl. Phys. Lett.* **89**, 2–5 (2006).
- Wakiya, N., Wang, J., Saiki, A., Shinozaki, K. & Mizutani, N. Synthesis and Dielectric Properties of $\text{Ba}_{1-x}\text{R}_{2x/3}\text{Nb}_2\text{O}_6$ (R: Rare Earth) with Tetragonal Tungsten Bronze Structure. *J. Eur. Ceram. Soc.* **19**, 1071–1075 (1999).
- Zhu, X. et al. A Crystal-chemical framework for relaxor versus normal ferroelectric behavior in tetragonal tungsten bronzes. *Chem. Mater.* **27**, 3250–3261 (2015).
- Liu, L., Wang, Y., Wang, Y. & Lv, R. Low-temperature dielectric anomalies in $\text{KSr}_2\text{Nb}_5\text{O}_{15}$ ceramics with tetragonal tungsten bronze structure: the effect of microstructure. *J. Alloys Compd.* **815** (2020).
- Labbe, P. Tungsten oxides, tungsten bronzes and tungsten bronze-type structures. *Key Eng. Mater.* **68**, 293 (1992).
- Whittle, T. A., Schmid, S. & Howard, C. J. Octahedral tilting in the tungsten bronzes. *Acta Crystallogr. B: Struct. Sci. Cryst. Eng. Mater.* **71**, 342–348 (2015).
- Campbell, B. et al. An algebraic approach to cooperative rotations in networks of interconnected rigid units. *Acta Crystallogr. A: Found. Adv.* **74**, 408–424 (2018).
- Zhang, L. L. & Huang, Y. N. Theory of relaxor-ferroelectricity. *Sci. Rep.* **10**, 1–18 (2020).
- Whittle, T. A., Howard, C. J. & Schmid, S. Structures and phase transitions in barium sodium niobate tungsten bronze (BNN). *Acta Crystallogr. B: Struct. Sci. Cryst. Eng. Mater.* **77**, 981–985 (2021).
- Grendal, O. G., Evans, D. M. & Aamlid, S. S. Revisiting the structures and phase transitions of $\text{Ba}_2\text{NaNb}_5\text{O}_{15}$. *J. Appl. Crystallogr.* **56**, 1456–1465 (2023).
- Torres-Pardo, A., Jiménez, R., González-Calbet, J. M. & García-González, E. Structural effects behind the low temperature nonconventional relaxor behavior of the $\text{Sr}_2\text{NaNb}_5\text{O}_{15}$ bronze. *Inorg. Chem.* **50**, 12091–12098 (2011).
- Gardner, J. & Morrison, F. D. A-site size effect in a family of unfilled ferroelectric tetragonal tungsten bronzes: $\text{Ba}_4\text{R}_{0.67}\text{Nb}_{10}\text{O}_{30}$ (R = La, Nd, Sm, Gd, Dy and Y). *Dalt. Trans.* **43**, 11687–11695 (2014).
- Ravez, J. Etude Comparative des Propriétés Cristallographiques, Dielectriques et d’optique Non Lineaire des Phases $\text{ABCNb}_5\text{O}_{15}$ (A = Ca, Sr, Ba, B = Ca, Sr, Ba, C = Na, K) de Type “Bronzes Oxygènes de Tungstène Quadratiques”. *J. Solid State Chem.* **5**, 239–246 (1972).
- Xu, S., Deng, Z., Shen, S., Wei, L. & Yang, Z. Structural and electrical effects of Ag substitution in tungsten bronze $\text{Sr}_2\text{Ag}_x\text{Na}_{1-x}\text{Nb}_5\text{O}_{15}$ ceramics. *Ceram. Int.* **46**, 13997–14004 (2020).
- Neurgaonkar, R. R., Oliver, J. R., Cory, W. K., Cross, L. E. & Viehlandt, D. Piezoelectricity in tungsten bronze crystals. *Ferroelectrics* **160**, 265–276 (1994).
- Campbell, B. J., Stokes, H. T., Tanner, D. E. & Hatch, D. M. ISODISPLACE: A web-based tool for exploring structural distortions. *J. Appl. Crystallogr.* **39**, 607–614 (2006).
- Stokes, H. T., Hatch, D. M. & Campbell, B. J. ISODISTORT, ISOTROPY Software Suite. iso.byu.edu.
- Miles, G. C., Stennett, M. C., Reaney, I. M. & West, A. R. Temperature-dependent crystal structure of ferroelectric $\text{Ba}_2\text{LaTi}_2\text{Nb}_3\text{O}_{15}$. *J. Mater. Chem.* **15**, 798–802 (2005).
- Campbell, B. J., Evans, J. S. O., Perselli, F. & Stokes, H. T. Rietveld refinement of structural distortion-mode amplitudes. *IUCr Comput. Comm. Newsl.* **8**, 81–95 (2007).
- Murata, T., Akamatsu, H., Hirai, D., Oba, F. & Hirose, S. Antiferroelectricity and robust dielectric response owing to competing polar and antipolar instabilities in tetragonal tungsten bronze $\text{K}_2\text{RNb}_5\text{O}_{15}$ (R: rare-earth). *Phys. Rev. Mater.* **4**, 1–11 (2020).
- Aamlid, S. S., Selbach, S. M. & Grande, T. Structural evolution of ferroelectric and ferroelastic barium sodium niobate tungsten bronze. *Inorg. Chem.* **59**, 8514–8521 (2020).
- Chen, J. et al. Zero thermal expansion in PbTiO_3 -based perovskites. *J. Am. Chem. Soc.* **130**, 1144–1145 (2008).
- Pan, Z. et al. Tolerance factor control of tetragonality and negative thermal expansion in PbTiO_3 -based ferroelectrics. *Chem. Mater.* **34**, 2798–2803 (2022).
- Chen, J. et al. Effectively control negative thermal expansion of single-phase ferroelectrics of PbTiO_3 -(Bi,Lu)FeO₃ over a giant range. *Sci. Rep.* **3**, 1–5 (2013).
- Neurgaonkar, R. R. et al. Growth and ferroelectric properties of tungsten bronze $\text{Sr}_{2-x}\text{Ca}_x\text{NaNb}_5\text{O}_{15}$ single crystals. *Mat. Res. Bull.* **23**, 1459–1467 (1988).
- Stephens, P. W. Phenomenological model of anisotropic peak broadening in powder diffraction. *J. Appl. Crystallogr.* **32**, 281–289 (1999).
- Levin, I. et al. Displacive order–disorder behavior and intrinsic clustering of lattice distortions in Bi-substituted NaNbO_3 . *Adv. Funct. Mater.* **30**, 1–13 (2020).
- Senn, M. S. et al. Structural origins of dielectric phenomena in promising Sr-Na-Nb-based TTB ferrorelaxors. *Inst. Laue-Langevin* (2023).
- Coelho, A. A. TOPAS and TOPAS-Academic: an optimization program integrating computer algebra and crystallographic objects written in C++. *J. Appl. Crystallogr.* **51**, 210–218 (2018).
- Petríček, V., Palatinus, L., Plášil, J. & Dušek, M. Jana 2020—a new version of the crystallographic computing system Jana. *Z. Krist. — Cryst. Mater.* **238**, 271–282 (2023).
- Kresse, G. & Hafner, J. Ab initio molecular dynamics for liquid metals. *Phys. Rev. B* **47**, 558–561 (1993).

42. Kresse, G. & Furthmüller, J. Efficiency of ab-initio total energy calculations for metals and semiconductors using a plane-wave basis set. *Comput. Mater. Sci.* **6**, 15–50 (1996).
43. Perdew, J. P. et al. Restoring the density-gradient expansion for exchange in solids and surfaces. *Phys. Rev. Lett.* **100**, 1–4 (2008).
44. Blöchl, P. E. Projector augmented-wave method. *Phys. Rev. B* **50**, 17953–17979 (1994).
45. Baroni, S., Gironcoli, S., de Corso, A. D. & Giannozzi, P. Phonons and related crystal properties from density-functional perturbation theory. *Rev. Mod. Phys.* **73**, 515–557 (2001).
46. Togo, A. & Tanaka, I. First principles phonon calculations in materials science. *Scr. Mater.* **108**, 1–5 (2015).
47. Gonze, X., Charlier, J. C., Allan, D. C. & Teter, M. P. Interatomic force constants from first principles: the case of α -quartz. *Phys. Rev. B* **50**, 13035–13038 (1994).
48. Gonze, X. & Lee, C. Dynamical matrices, Born effective charges, dielectric permittivity tensors, and interatomic force constants from density-functional perturbation theory. *Phys. Rev. B: Condens. Matter Mater. Phys.* **55**, 10355–10368 (1997).
49. Stokes, H. T., Hatch, D. M. & Campbell, B. J. FINDSYM, ISOTROPY Software Suite.
50. Stokes, H. T. & Hatch, D. M. FINDSYM: Program for identifying the space-group symmetry of a crystal. *J. Appl. Crystallogr.* **38**, 237–238 (2005).
51. Tidey, J. P. et al. Structural origins of dielectric anomalies in the filled tetragonal tungsten bronze $\text{Sr}_2\text{NaNb}_5\text{O}_{15}$ —Data Upload. *figshare. Dataset*. <https://doi.org/10.6084/m9.figshare.24279499.v1> (2024).

Acknowledgements

The authors thank T. Brown, C.M. King, A.P. Brown and S.J. Milne for supplying the SNN ceramic and associated electrical data. We also thank S. Simpson and B.R.M. Tragheim for assistance in collecting DLS data, and S. Simpson, E. Ladbrook and B.R.M. Tragheim for ILL data. This work was carried out under the EPSRC grant “New directions in high temperature dielectrics: unlocking performance of doped tungsten bronze oxides through mechanistic understanding” (EP/V053701/1). X-ray powder diffraction data were collected as part of the “Oxford/Warwick Solid State Chemistry BAG to probe composition-structure-property relationships in solids” at beamline I11, Diamond Light Source (CY25166). Synchrotron X-ray powder diffraction data were also collected at Taiwan Photon Source, National Synchrotron Radiation Research Center, with beamtime 2021-2-126. The neutron powder diffraction data was collected at D2B, Institut Laue-Langevin under proposal 5-23-783. MSS acknowledges the Royal Society for a University Research Fellowship (UF160265). WTC acknowledges the National Science and Technology Council, Taiwan, for funding 111-2112-M-002-044-MY3, 112-2124-M-002-012, and Academia Sinica project number AS-iMATE-113-12. This work made use of the facilities of the N8 Centre of Excellence in Computationally Intensive Research (N8 CIR) provided and funded by the N8 research partnership and EPSRC (Grant No. EP/T022167/1). The Centre is co-ordinated by the Universities of Durham, Manchester, and York. UD and NCB acknowledge the Leverhulme Trust for

a research project grant (Grant No. RPG-2020-206). This work made use of the ARCHER2 UK National Supercomputing Service (<https://www.archer2.ac.uk>).

Author contributions

The project was conceived by M.S.S., N.C.B., and R.B., and led by J.P.T. and M.S.S. Electron experiments were performed by J.P.T., A.M.S., and R.B.; first-principles calculations by U.D. and N.B.; TPS synchrotron experiments by W.T.C., B.H.C., and Y.C.C.; ILL neutron experiments by M.S.S. and MTFD; DLS synchrotron experiments prepared by J.P.T. and ran as part of Block Allocation Group access. Experimental data analysis was led by J.P.T. with support from M.S.S., R.B., and A.M.S.; first principles calculations data analysis led by U.D. and N.C.B. Authorship of the manuscript was led by J.P.T. with significant contributions from U.D., M.S.S., R.B., and N.C.B.; all authors contributed to and approved of the final manuscript.

Competing interests

The authors declare no competing interests.

Additional information

Supplementary information The online version contains supplementary material available at <https://doi.org/10.1038/s43246-024-00508-1>.

Correspondence and requests for materials should be addressed to Jeremiah P. Tidey or Mark S. Senn.

Peer review information *Communications Materials* thanks the anonymous reviewers for their contribution to the peer review of this work. Primary Handling Editors: Andreja Benčan Golob and Aldo Isidori. A peer review file is available.

Reprints and permissions information is available at <http://www.nature.com/reprints>

Publisher's note Springer Nature remains neutral with regard to jurisdictional claims in published maps and institutional affiliations.

Open Access This article is licensed under a Creative Commons Attribution 4.0 International License, which permits use, sharing, adaptation, distribution and reproduction in any medium or format, as long as you give appropriate credit to the original author(s) and the source, provide a link to the Creative Commons licence, and indicate if changes were made. The images or other third party material in this article are included in the article's Creative Commons licence, unless indicated otherwise in a credit line to the material. If material is not included in the article's Creative Commons licence and your intended use is not permitted by statutory regulation or exceeds the permitted use, you will need to obtain permission directly from the copyright holder. To view a copy of this licence, visit <http://creativecommons.org/licenses/by/4.0/>.

© The Author(s) 2024